Antenna–Filter–Antenna Arrays as a Class of Bandpass Frequency-Selective Surfaces

Abbas Abbaspour-Tamijani, *Member, IEEE*, Kamal Sarabandi, *Fellow, IEEE*, and Gabriel M. Rebeiz, *Fellow, IEEE*

***Abstract*—A method is introduced for designing bandpass frequency-selective surfaces (FSSs) using arrays of antenna–filter–antenna (AFA) modules. An AFA module is a filter with radiation ports, which is obtained by integrating two antennas and a nonradiating resonant structure in between. AFA modules are designed based on circuit models and microwave filter design techniques. Three types of these AFA modules are designed using microstrip antennas and coplanar-waveguide resonators, and are used to form FSSs with three- and four-pole shaped bandpass response at 35 GHz. FSS structures are formed by arraying these modules in a periodic grid with an optimal cell size. The proposed concept and the design method are validated using numerical simulation (finite-element method), as well as experimental results.**

***Index Terms*—Antenna–filter–antenna (AFA), , bandpass filter, frequency-selective surface (FSS), high-order FSS.**

I. Introduction

FREQUENCY-SELECTIVE surfaces (FSSs) can be viewed as filters with radiative ports, which are generally realized using planar periodic structures. High-order filters are commonly designed using multilayer FSS structures [1], [2]. Since computational complexity drastically increases for multiple layers, design of the high-order FSSs is performed by combining the individually designed FSS layers. The FSS layers, acting as individual resonators, are stacked using thick (0.2–$0.3\lambda_0$) dielectric slab spacers, which can be considered as simple impedance inverters, to form multipole filters. However, there are several problems with this method. First, the resulting filter topology as a chain of resonators and inverters is suitable only for a limited class of filter responses, which reduces the design space considerably. Second, the direct near-field coupling between the FSS layers in the stack and the loading effect of the dielectric slabs can invalidate the simple resonator-inverter interpretation. As a result, the filter synthesis methods offer only a rough first-pass design, and the design procedure generally has to be followed by retuning the individual FSS layers and dielectric slabs using elaborate optimization methods. Third, the overall stacked structure can be thick and bulky, which is not desirable for many applications.

Manuscript received October 15, 2003; revised March 10, 2004.

A. Abbaspour-Tamijani was with The Radiation Laboratory, Department of Electrical Engineering and Computer Science, The University of Michigan at Ann Arbor, Ann Arbor, MI 48109-2122 USA. He is now with the Department of Electrical Engineering, Arizona State University, Tempe, AZ 85287-5706 USA.

K. Sarabandi and G. M. Rebeiz are with The Radiation Laboratory, Department of Electrical Engineering and Computer Science, The University of Michigan at Ann Arbor, Ann Arbor, MI 48109-2122 USA (e-mail: saraband@eecs.umich.edu; rebeiz@eecs.umich.edu).

Digital Object Identifier 10.1109/TMTT.2004.831572

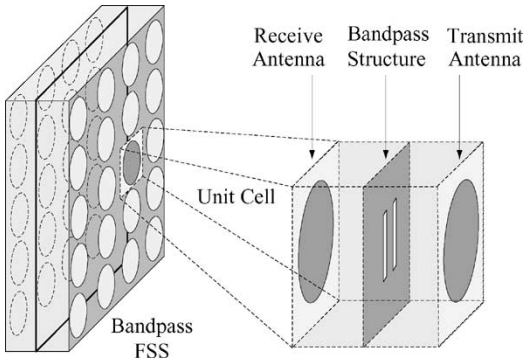

Fig. 1. AFA array composed of patch antennas and CPW resonators.

Alternatively, frequency selectivity can be achieved by using an array of antenna–filter–antenna (AFA) modules [3]. Each AFA module is composed of a receive antenna, a nonradiating resonant structure, and a transmit antenna. This concept is similar to using antenna–amplifier–antenna elements to form quasi-optical amplifier arrays [4], or antenna–delay line–antenna elements to form discrete lens arrays [5]. However, a different type of delicacy is involved when the frequency response is of primary concern. Also, as compared to the standard approach, the AFA method can be used to synthesize a more general category of the filtering shapes. A simple example of an AFA-based FSS has been proposed in [1] (based on an earlier work [6]), where a pseudo-high-pass filter is formed between the input and output apertures of an array of open-ended waveguides.

Fig. 1 shows the case where the radiative elements in the AFA modules are two back-to-back microstrip patch antennas, and the middle resonant structure is an ensemble of coplanar-waveguide (CPW) resonators, fabricated in the common ground plane (referred to as the CPW layer). The antennas and CPW resonant structure are coupled at localized coupling points, where the CPW geometry is altered so as to carry a net magnetic current (the net magnetic current in a symmetric continuous CPW line is zero). The coupling, therefore, can be achieved through short slots, open-ended CPW lines, or step variations in the width of the CPW lines. If resonant-type radiative elements are used, each antenna element can be considered as a combination of a radiative resistance and a resonator. Since these built-in resonators function as the first and last resonators of the filter, formed between the radiative ports (Fig. 2), for a given filter order N, the required number of CPW resonators reduces to $N-2$. A special case of this structure is used in [7], where two patch antennas are coupled through a nonresonant slot to form a two-pole bandpass filter. As opposed to the conventional stacked FSS designs, a higher

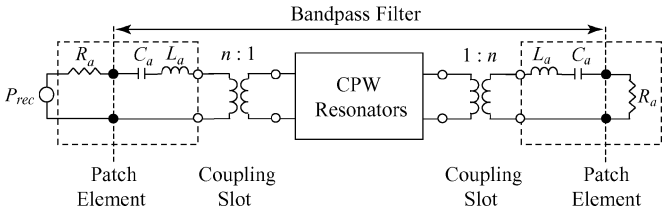

Fig. 2. AFA as a bandpass filter between two radiative ports.

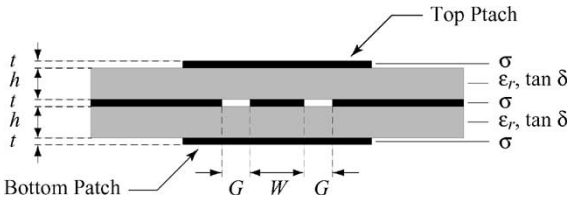

Fig. 3. Layer structure used in the AFA designs.

order response can be obtained simply by adding resonators in the CPW layer, instead of increasing the number of layers.

Developing an FSS design methodology based on the described type of AFA modules is the main subject of this paper. The following sections describe the design, modeling, fabrication, and measurement of several types of AFAs and FSS structures.

II. Design of the AFA Modules

As soon as the circuit models of the antennas and coupling slots are extracted and their role in the filter topology is understood, designing the AFA modules is streamlined using microwave filter design techniques. The design method and some possible topologies are presented through three illustrative examples.

A. Type-I AFA: Three-Pole Chebyshev Bandpass

According to the circuit model shown in Fig. 2, the first and last resonators and the input/output coupling of the bandpass AFA depend solely on the choice of the radiative element. The input/output couplings of the filter are related to the external Q ($Q_{\rm ext}$) of the first and last resonators [8], which, for lossless resonant patch elements, can be written as [9]

$$Q_{\rm ext} = \frac{2\pi f_0 L_a}{R_a} = \frac{1}{2\pi f_0 C_a R_a} \tag{1}$$

where f_0 is the resonant frequency, and R_a, L_a, and C_a are determined from the equivalent RLC circuit model of the antenna. For the case of patch antennas, the substrate thickness is particularly important in achieving the desired value of $Q_{\rm ext}$: the thicker the substrate, the lower $Q_{\rm ext}$ and the wider the passband. Also, the geometry of the patch element can slightly affect the value of $Q_{\rm ext}$. For a 35-GHz hexagonal patch element on a 500-μm-thick 7740 Corning glass substrate ($\varepsilon_r = 4.45, \tan\delta = 0.006$), the estimated value of the external Q is 15.6 (obtained by a lossless finite-element method (FEM) simulation[1]). Based on the design equations in [8], this can be used to synthesize a three-pole Chebyshev filter with a fractional bandwidth of up to nearly 10% and a passband ripple of $\leq$ 0.45 dB ($>$ 10-dB return loss).

The couplings between the antennas and CPW resonators are also very important and have to be realized in a controlled and localized fashion. Discontinuities, bends, or any geometrical deformations in the CPW lines that result in a net magnetic current can generate parasitic coupling mechanisms and must be avoided.

[1]High Frequency Structure Simulator (HFSS), Ansoft Corporation, Pittsburgh, PA, 2003.

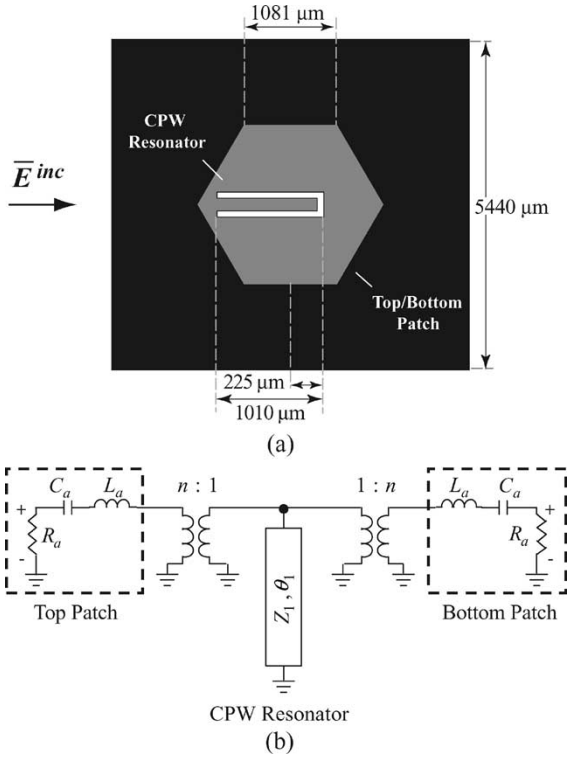

Fig. 4. Type-I AFA. (a) Layout. (b) Circuit model. Top and bottom patch antennas lie exactly on top of each other.

To simplify the design task, the same type of patch element and layer structure is used for all designs that will be considered here. The CPW resonators have the cross-sectional dimensions of G/W/G = 50/100/50 μm with a metal thickness of t = 3 μm (Fig. 3).

The first design is a three-pole Chebyshev bandpass AFA with 8% bandwidth at 35 GHz [see Fig. 4(a)]. This AFA, which we refer to as Type I, is composed of two patch antennas and a quarter-wave CPW resonator. The CPW resonator is coupled to the fundamental resonant mode in each patch through its open end. The equivalent circuit consists of two series *LC* resonators, and a shunt stub that presents a parallel resonance at the center frequency [see Fig. 4(b)]. In practice, due to the finite inductance of the shorted end, the physical length of the shunt stub is slightly less than $\lambda_g/4$ (λ_g is the CPW guided wavelength).

The model parameters for the Type-I AFA are given in Table I. The parameters in the antenna model can be extracted from the simulation of the antenna and coupling slot in an infinite structure. The real design parameter after fixing the antenna and CPW line dimensions is the value of coupling between the antennas and resonator (or, equivalently, n), which is controlled by the position of the coupling slot with respect to the center of the

TABLE I
MODEL PARAMETERS FOR THE TYPE-I AFA AT 35 GHz

R_a (Ω)	50	n	0.196
L_a (nH)	3.7	Z_1 (Ω)	65
C_a (fF)	5.6	θ_1 (deg.)	90

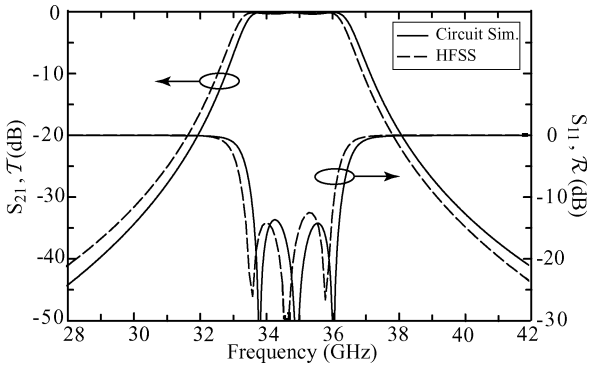

Fig. 5. Simulated S-parameters of the Type-I AFA using the circuit model in Fig. 4(b). HFSS simulations show the reflection and transmission coefficients for a periodic array of such elements (see Section III-B).

patch. Fig. 5 presents the simulated S-parameters based on the circuit model. S_{21} and S_{11} represent the ratio of the transmitted and reflected power to the total power received by a single AFA cell (P_{rec}). The proposed circuit model and the resulting frequency response are only valid for a normal incident wave with the electric field polarized in parallel to the CPW resonator. This polarization will be hereforth referred to as the principal polarization for this structure.

B. Type-II AFA: Three-Pole Bandpass With a Transmission Zero

The geometry of the Type-II AFA cell is shown in Fig. 6 along with its equivalent-circuit model. This AFA has an equiripple response in the passband and an attenuation zero in the lower rejection band. A handful of topologies may be considered to realize transmission zeros, but what makes this design interesting is the presence of a 180° phase shift between its input and output at the center frequency.

The Type-II AFA is composed of two patches and a half-wave short-ended CPW resonator. The patches are coupled to the resonator through flared ends of the CPW gaps, which form two coupling slots. The phase translation is achieved by moving each patch toward one end of the resonator and coupling it to a different slot. In the fundamental resonant mode, the magnetic currents generated in these slots are out-of-phase, resulting in a 180° phase difference between the receive and transmit patches. Although the dominant coupling to each patch is through the slot that lies inside its resonance region (represented by the transformers with the turn ratio n_1), it also receives a residual coupling through the opposite slot, which interacts with its fringe field (represented by the transformers with the turn ratio n_2). Presence of this parallel signal path is, in fact, responsible for the existence of the transmission zero in the lower rejection band. As the dominant and residual couplings take place at different locations, a transmission line (Z_0, θ_0) is introduced in the

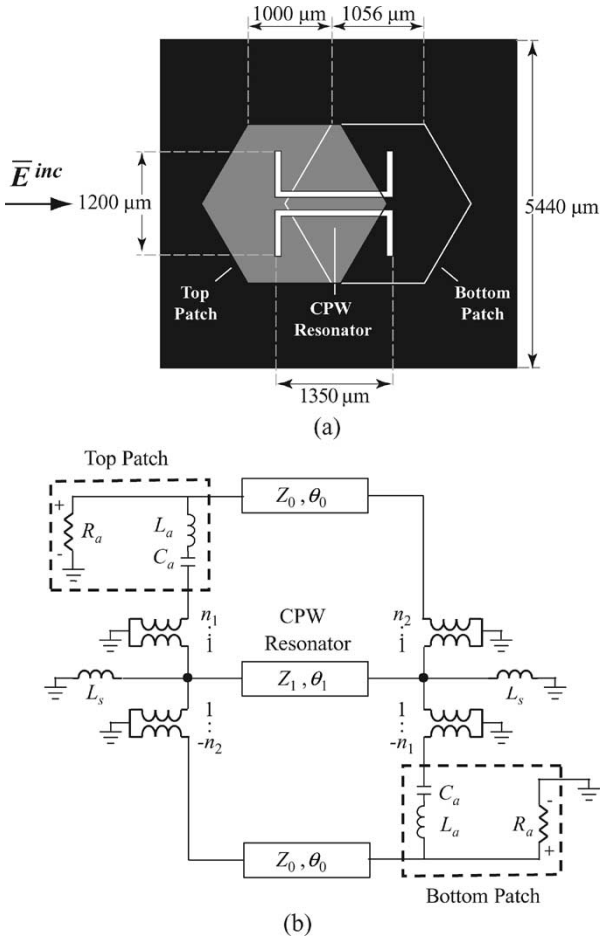

Fig. 6. Type-II AFA. (a) Layout. (b) Circuit model.

model to account for the resulting phase difference, as shown in Fig. 6(b). Due to the out-of-phase nature of these two coupling mechanisms, which reduces the net amount of coupling between the antennas and CPW resonator, the coupling slots have to be designed significantly longer than in the Type-I AFA. The long slots present a considerable self-inductance, which is included in the model by adding inductors to the ends of the CPW resonator. Presence of these inductors modifies the resonant length of the half-wave resonator. The long slots also increase the length of the current path in the patch ground plane, and the patches need to be made smaller to compensate for the resulting change in the resonant frequency.

The design process for the Type-II AFA includes finding the lengths of the coupling slots and CPW resonator, and the relative location of the patch elements. As these parameters are generally linked in the physical layout, the design task requires more optimization through full-wave simulation. However, the circuit model proves extremely helpful in understanding the effect of the geometrical parameters. The values of the model parameters for an 8% bandpass filter at 35 GHz are given in Table II. Fig. 7 shows the simulated S-parameters for the Type-II AFA. Again, the model and simulated response are valid only for the incident waves with principal polarization, which is defined similar to the previous example. The simulated S_{21} has a transmission zero in the lower rejection band at 32.0 GHz.

TABLE II
MODEL PARAMETERS FOR THE TYPE-II AFA AT 35 GHz

R_a (Ω)	50	n_2	0.089
L_a (nH)	3.82	Z_0 (Ω)	50
C_a (fF)	5.6	θ_0 (deg.)	107.9
L_s (pH)	210	Z_1 (Ω)	65
n_1	0.431	θ_1 (deg.)	107.9

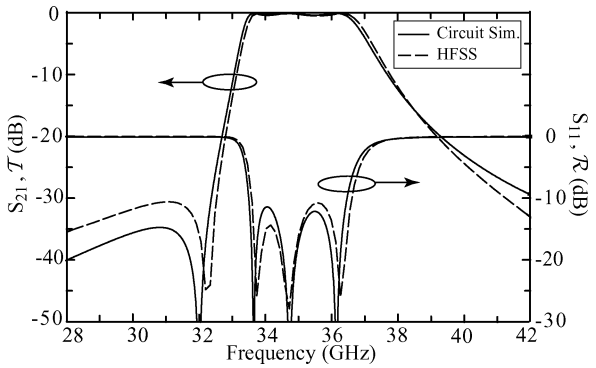

Fig. 7. Simulated S-parameters of the Type-II AFA using the circuit model in Fig. 6(b). HFSS simulations show the reflection and transmission coefficients for a periodic array of such elements (see Section III-B).

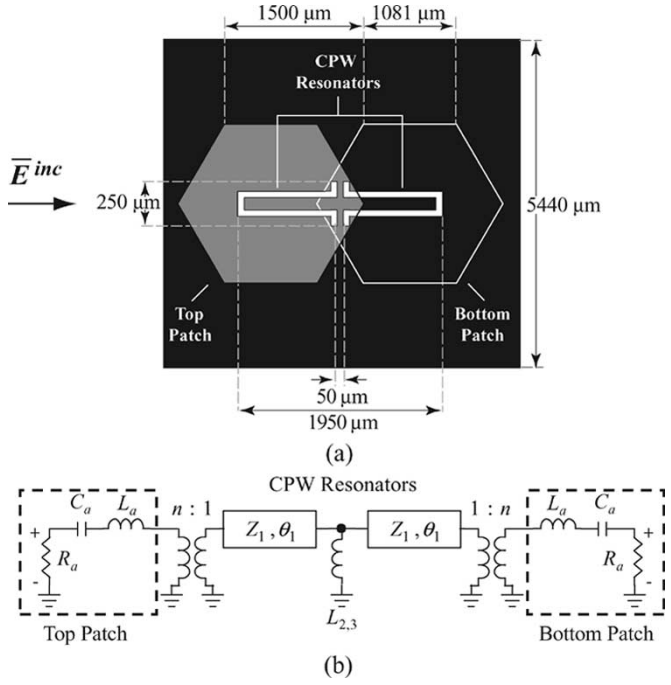

Fig. 8. Type-III AFA. (a) Layout. (b) Circuit model.

C. Type-III AFA: Four-Pole Chebyshev Bandpass

A four-pole AFA is obtained by using two quarter-wave resonators in the CPW layer [see Fig. 8(a)]. Each resonator in the Type-III AFA is coupled to only one of the antennas through its open end (similar to Type-I), and the coupling between the two resonators is achieved through shunt inductors at their common end. The inductors are realized using high-impedance lines between the center conductor and coplanar ground [10].

TABLE III
MODEL PARAMETERS FOR THE TYPE-III AFA AT 35 GHz

R_a (Ω)	50	n	0.196
L_a (nH)	3.7	Z_1 (Ω)	65
C_a (fF)	5.6	θ_1 (deg.)	87.7
$L_{2,3}$ (pH)	12		

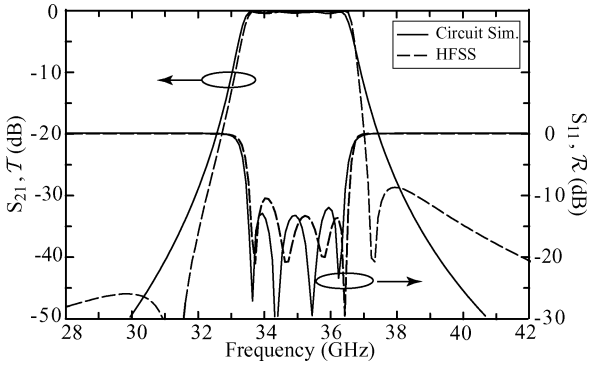

Fig. 9. Simulated S-parameters of the Type-III AFA using the circuit model in Fig. 8(b). HFSS simulations show the reflection and transmission coefficients for a periodic array of such elements (see Section III-B).

These inductors result in no net magnetic current and, hence, do not generate any unwanted coupling to the antennas.

The circuit model of the Type-III AFA is shown in Fig. 8(b). The locations of the coupling gaps are determined for the required value of coupling (or, equivalently, n), similar to the Type-I design. The value of the coupling inductor $L_{2,3}$ is simply determined from standard inverter design formulas [8]. The resonator length (θ_1) must then be modified to account for the self-inductance of the coupling inductor [10], [11].

The model parameters for an 8.5% Chebyshev bandpass filter at 35 GHz and the simulated S-parameters are presented in Table III and Fig. 9, respectively. As expected, increasing the order of the filter results in a faster rolloff in the rejection band.

III. AFA-BASED FSSs

Once the AFA modules are designed, it is straightforward to form the FSS by arranging these modules in a periodic array. However, the frequency response of the FSS will not follow that of the AFA modules, unless a particular choice of the cell size is applied.

A. Effect of the Cell Size

As it was mentioned earlier, the filtering action of the AFA is performed only on the portion of the incident power that is received by the module (P_{rec}). This power is ultimately limited by the radiative aperture of the receive antenna A_r defined as [9]

$$A_r(\vartheta,\varphi) = \frac{\lambda^2}{4\pi} D(\vartheta,\varphi) \tag{2}$$

where λ is the free-space wavelength at the center frequency and $D(\vartheta,\varphi)$ represents the directivity of the antenna in the direction

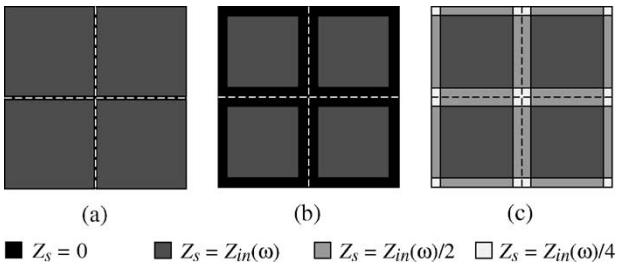

Fig. 10. Representation of four unit cells in a periodic array of impedance panels. (a) $A_r = A_c$. (b) $A_r < A_c$. (c) $A_r > A_c$. Cell boundaries are shown via dashed lines. $A_c \equiv$ cell area; $A_r \equiv$ effective radiative aperture.

of incidence (ϑ, φ).[2] A single AFA element on an infinite ground plane can be viewed as a window of area A_r and impedance $Z_s = Z_{\text{in}}(\omega)$. $Z_{\text{in}}(\omega)$ is the input impedance presented by the AFA element, it is matched in the passband and reactive in the rejection band.

The above intuitive interpretation suggests that the periodic array has to have a cell area equal to A_r in order to maintain the frequency response of the constituent AFA elements. A pictorial demonstration of the underlying concept is presented in Fig. 10. Although a rigorous proof of this requirement is not available in the general case,[3] it can be shown that this is, in fact, the *necessary condition* for the case of the resonant AFA elements placed on a rectangular grid.

For the AFA examples in Section II, the simulated directivity of the patch antenna at boresight is $D(0,0) = 7.04$ dBi at 35 GHz,[4] resulting in an effective radiative aperture of $A_r = 29.6$ mm^2 for the normal incidence. Therefore, an optimal square cell must have a side length of $l_c = 5.44$ mm for these elements.

The fact that the FSS cell size has to be chosen equal to A_r can present a problem in applications where the FSS is considered for large incidence angles. For the microstrip patch antennas with a directivity of 6–8 dBi, the optimal A_c results in a cell side length of $l_c > 0.56\lambda_0$, for which the periodic structure is prone to carrying surface-wave modes at frequencies not far from the passband [1]. These surface-wave modes create strong transmission zeros, which can be dragged into or near to the passband for some oblique angles of incidence, resulting in an excessive transmission loss or a distorted frequency response. With $l_c = 5.44$ mm and for E-plane incidence at $\vartheta = 0°, 15°$, and 30°, for instance, the first surface-wave null appears at 49, 41.2, and 35.5 GHz, respectively. This limits the operation of the resulting FSS to angles of $\vartheta < 30°$ in the E-plane. For a plane wave incident in the H-plane, however, the surface-wave modes are not strongly excited, and a larger range of operation can be achieved.

The surface-wave nulls can be somewhat deterred by using low-directivity elements with smaller A_r and closer placement of the AFA modules in the array. However, the techniques for reducing directivity, such as using small antennas on high-permittivity substrates, may prove useless, as increasing the dielectric constant tends to lower the frequency of the surface-wave modes.

[2]Although it is not obvious from (1), A_r is generally related to the physical dimensions of the antenna and has no strong dependence on frequency.

[3]The authors are not aware of this subject in the open literature.

[4]Advanced Design System, Agilent Technologies, Santa Clara, CA, 2002.

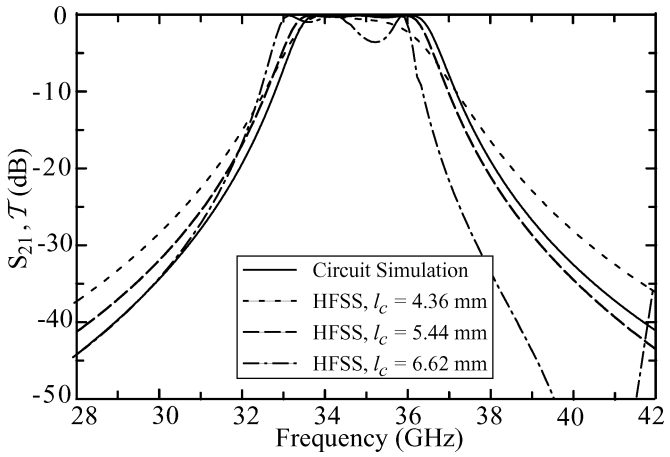

Fig. 11. FEM simulation of the Type-I FSS using different values of l_c. Circuit simulation is also shown for comparison.

B. Finite-Element Simulation

When the cell size is determined, an FEM simulation of the structure can be performed based on the periodic boundary conditions. For normal incidence and the electric field polarized in parallel with one of the FSS grid axes, the periodic boundary conditions may be replaced by the perfect electric conductor (PEC) and perfect magnetic conductor (PMC) walls to reduce the computational complexity. The layer structure presented in Fig. 3 is used, and the thickness of the metal layer and the losses in the dielectric substrate and conductors are neglected at this stage. A commercial FEM simulator, such as HFSS, is generally capable of handling such a simulation effectively. With a well-designed AFA element, this usually results in a reasonable FSS frequency response in the first attempt. The final tuning of the layout, if necessary, can be performed by an insightful tweaking of some critical dimensions and is based on FEM simulations.

The FEM simulation of the reflection and transmission coefficients of the FSS obtained by arraying Type-I AFA elements with $l_c = 5.44$ mm are shown in Fig. 5. These simulations clearly match the circuit-based S-parameters of the AFA, also shown in the same plot. Fig. 11 shows the FEM simulations repeated for 20% larger and 20% smaller l_c. It is evident that, only for the optimal value of $l_c = \sqrt{A_r}$, the FSS achieves the desired frequency response. According to the FEM simulations, for $l_c = 5.44$ mm, the surface-wave null is located at 48 GHz. For $l_c = 6.62$ mm, this null moves to 41 GHz, as can be seen in Fig. 11.

Similarly, FSSs can be formed based on the Type-II and Type-III AFAs and using the optimal cell size. The FEM simulation closely follows the AFA-based analysis for the Type-II FSS (Fig. 7), but shows a noticeable discrepancy for the case of the Type-III FSS (Fig. 9), in which the simulated transmission coefficient contains two out-of-band transmission zeros, not predicted using the AFA model. A closer inspection of the AFA geometry in Fig. 8 suggests formation of a direct

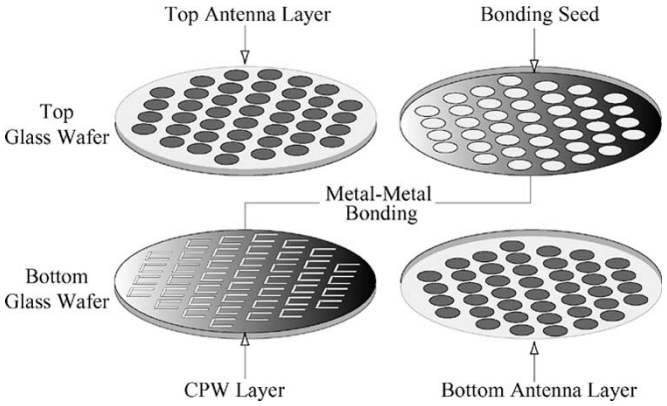

Fig. 12. Detailed description of the physical layers in a laboratory fabricated prototype.

coupling of the input/output signals (waves) to the quarter-wave CPW resonators, which are prone to radiation at their exposed open ends. These direct couplings, which are not included in the AFA model of Fig. 8(b), create parallel signal paths, which are responsible for the presence of the transmission zeros.

IV. FSS Fabrication and Measurement

Choice of the fabrication process for the AFA-based FSSs is particularly important at millimeter-wave frequencies, for at least two reasons, which are: 1) geometrical tolerances and 2) stacking imperfections. Performing accurate FSS measurements is also a hard task at these frequencies. These two issues are addressed and some experimental results are presented here.

A. Fabrication

Due to the small dimensions at Ka-band frequencies, the accuracy required for the CPW layer is approximately ± 2 μm. Therefore, a fabrication process based on thin-film technology should be used, as shown in Fig. 12. Each FSS sample is fabricated using two 500-μm-thick 7740 Corning (Pyrex) glass wafers. First, the patch antennas are deposited on the two wafers using an evaporated film of Ti(800 Å)/Au(5000 Å), and a liftoff process. These patches are then electroplated with Au to a thickness of 3–5 μm. Next, the CPW and bonding seed layers are deposited on the other side of the wafers using a second evaporated Ti(500 Å)/Au(5000 Å) layer. The bonding seed layer is a metallic grid that entirely overlaps with the CPW ground plane in the final stack. This layer has no electromagnetic function, and is merely used to facilitate metal-to-metal bonding of the wafers. The CPW layer is then electroplated to 3 μm, which is approximately five times the skin depth at 35 GHz ($\sigma = 3.8 \times 10^7$ S/m). The bonding seed layer is left intact.

The final fabrication step is to stack the two processed wafers. Most adhesives are lossy at millimeter-wave frequencies and, even if the loss can be neglected, the thickness of the adhesive layers is not accurately controllable and can have a negative impact on the performance of the FSS. An alternative approach is using a thermo-compression bonding process [12]. In this process, the top and bottom wafers are aligned and the bonding is formed between the gold in the CPW and bonding seed layers by applying a pressure of 40–50 N/cm^2 at the temperature of 390 °C. This temperature can be readily endured by the Pyrex glass wafers (strain point $= 510\,^{\circ}$C, softening point $= 821\,^{\circ}$C).

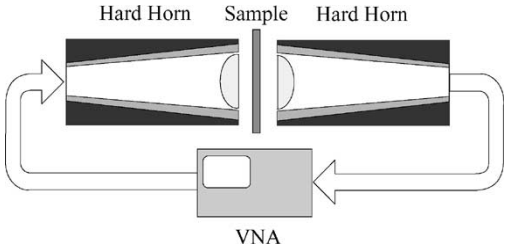

Fig. 13. Free-space measurement system using hard horns of [15].

B. Measurement Method

Quasi-optical measurement systems have been used by a number of researchers at 60–300 GHz [13], [14], but the required lens/mirror size and focal length prove impractical at Ka-band. Based on the hard horns developed by Ortiz *et al.* [4] and Ali *et al.* [15], a guided measurement system can be formed that simulates an oversized parallel-plate waveguide. Hard horns are antennas with nearly uniform aperture distribution, which are formed by dielectric loading of the metallic pyramidal horns. A dielectric lens added to each hard horn to compensate for the spherical phase error across its aperture. In the measurement system shown in Fig. 13, the hard horns form two parallel TEM ports, which are separated by an air gap, and the sample under test is placed in the middle of these two ports. As the sample can be freely reoriented in the air gap, this setup proves convenient for performing measurements at arbitrary angles of incidence and different polarizations.

Since the electromagnetic field in the gap region is assumed to be predominantly TEM, the air gaps between the hard-horn apertures and the surfaces of the sample can be treated as transmission-line sections. This allows for a standard thru-reflect-line (TRL) calibration of the measurement setup, which simultaneously deembeds the connecting cables, hard horns, and the air gaps from the measurement [16]. A time-gating process is also applied to filter out the residual error due to the multiple reflections of the high-order modes not included in TRL calibration.

C. Measurement Results

Samples of the Type-I and Type-II FSSs were fabricated and tested at The University of Michigan at Ann Arbor. Although the initial samples had the general form of the desired frequency response, the measured results were considerably different from the simulations (not shown). A close examination of the fabricated arrays revealed the source of this discrepancy. In the simulations, the CPW layer are considered to be immersed in a homogeneous dielectric medium of $\varepsilon_r = 4.45$. However, as it can be seen from the layer structure in Fig. 3, due to the finite thickness of the gold CPW lines ($t \approx 3$ μm), a portion of the CPW gaps is filled with air. Also, the bonding seed layer is 0.5–0.6-μm thick, and creates an air gap between the top wafer and CPW metal layer (see Fig. 12). Although very thin, presence of these air regions at the location of the highest electric-field intensity results in a measurable reduction in the effective dielectric constant of

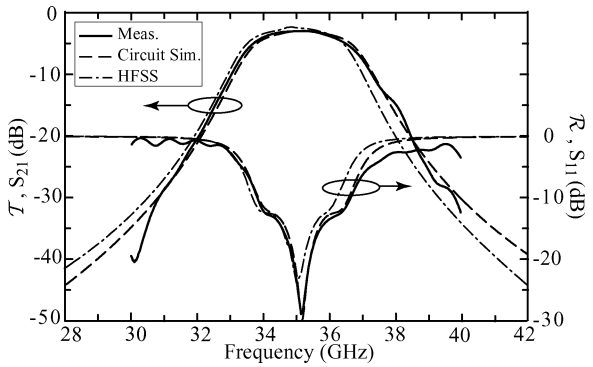

Fig. 14. Measured and simulated frequency response of the Type-I FSS for normal incidence with the principal polarization.

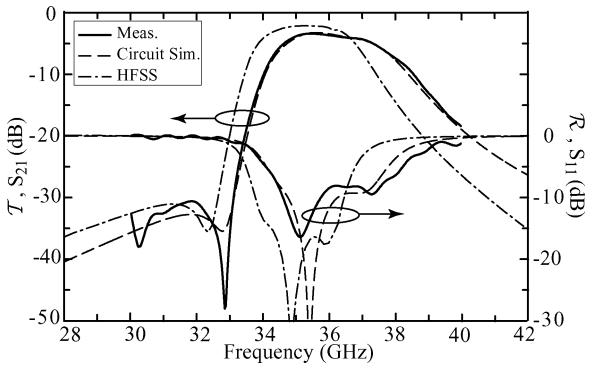

Fig. 15. Measured and simulated frequency response of the Type-II FSS for normal incidence with the principal polarization.

the CPW lines. Fitting the circuit model simulations and measured data for the first set of samples of the Type-I and Type-II FSS resulted in $\varepsilon_{r-\text{eff}} = 4.15$. Based on this observation, the lengths of the CPW resonators were adjusted and new FSS samples were fabricated. The layout dimensions in Figs. 4(a) and 6(a) indicate these modified values.

The measured and simulated reflection and transmission coefficients of the Type-I FSS for normal incidence in the principal polarization are presented in Fig. 14. The measured data are given for the 30–40-GHz band, which is the range of operation of the measurement setup. A passband response with 1-dB bandwidth of 8.2% centered at 35.1 GHz, and a mid-band insertion loss of 3.0 dB are measured. Circuit simulations can be repeated based on the model in Fig. 4(b) with the values of Z_1 and θ_1 modified for $\varepsilon_{r-\text{eff}} = 4.15$. After adding a series resistor of $r_a = 7.0\ \Omega$ to the antenna model and an attenuation coefficient of $\alpha_1 = 1.7$ dB/cm to the CPW transmission line, the circuit simulations show a perfect match with the measurement. This is equivalent to an antenna efficiency of 88%, and an unloaded Q of 38 for the CPW resonator. Fig. 14 also presents the FEM simulations after introducing a finite conductivity of $\sigma = 3.8 \times 10^7$ S/m (for the electroplated gold) and a dielectric loss tangent of $\tan\delta = 0.006$. From the total of 3.0-dB insertion loss at the mid-band frequency, 1.3 dB is due to the losses in the dielectric substrates, and the rest is due to the ohmic losses in the metallic structure, which is mainly contributed from the CPW resonator.

Fig. 15 shows the measured and simulated frequency response for the Type-II FSS for normal incidence in the principal polarization. The passband is 8.2% wide and is centered at 36.0 GHz. Although the layout of this design was also modified for $\varepsilon_{r-\text{eff}} = 4.15$, later matching of the circuit simulations to the measured data resulted in a dielectric constant of $\varepsilon_{r-\text{eff}} = 4.00$ for the CPW line, which explains the 3% detuning of the passband. This could be caused by higher thicknesses of the gold in the CPW layer or the air gap between the top wafer and CPW metallization. The presented circuit simulations are based on the model in Fig. 6(b) with values of Z_1 and θ_1 adjusted for $\varepsilon_{r-\text{eff}} = 4.00$, and losses added in the antennas, CPW resonator, and series inductors ($r_a = 7.0\ \Omega$, $\alpha_1 = 1.7$ dB/cm, $r_s = 2.2\ \Omega$). The measured mid-band insertion loss is 3.5 dB, in this case, from which 1.2 dB is a result of the dielectric losses and the rest is due to the conductor loss in the CPW structure and antennas. There is no clear explanation why the measured insertion loss does not match the FEM simulation, but it can be due to the same type of fabrication imperfections that cause the detuning of the passband.

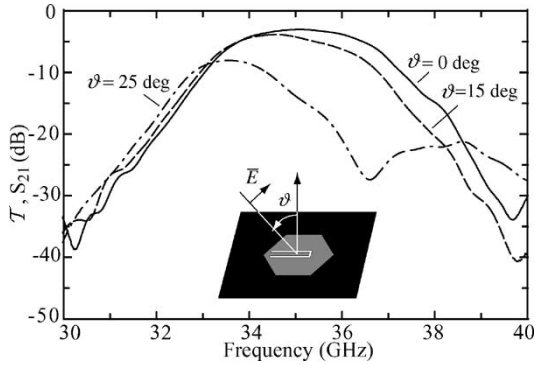

Fig. 16. Measured transmission coefficient of the Type-I FSS for three different values of the angle of incidence.

To examine the angular range of operation, the measurement of the Type-I FSS was repeated for the incidence angles of $(\vartheta, \varphi) = (15°, 0)$ and $(25°, 0)$. The resulting transmission coefficients are presented in Fig. 16 along with the measured response for the normal incidence. As expected, the transmission coefficient quickly deteriorates with increasing the angle of incidence. At $\vartheta = 25°$, the transmission null is located at 36.5 GHz, which is practically inside the passband.

V. Conclusion

Using periodic arrays of the AFA modules has been proposed as a new method to design high-order bandpass FSSs with a shaped frequency response. The flexibility of this method stems from the fact that the AFA modules can be designed as individual elements based on filter synthesis techniques. This results in an effective design method, which requires a minimal number of full-wave simulations. The AFA method can be used to form frequency responses that are more general than what could be achieved using stacked FSS designs. Also, the AFA-based FSSs have a simple layer structure and a much smaller overall thickness. However, as the cell size cannot be made arbitrarily small, the FSS structure can easily support surface-wave resonant modes that are close to the passband at oblique angles

of incidence, resulting in a narrow angular range of operation ($\vartheta \leq \pm 20^\circ$ in the E-plane). Also, since the AFA modules are generally polarization sensitive, designing a dual-polarized FSS based on this technique also requires packing two single-polarized AFA elements in each cell. In spite of these limitations, the AFA arrays may be considered for applications where the incoming signal is collimated and linearly polarized. They are expected to find application in designing radomes for high-gain antennas, multifeed shared-aperture antennas, high-impedance reactive surfaces, and waveguide bandpass filters.

ACKNOWLEDGMENT

The authors would like to thank M. Manteghi, University of California at Los Angeles (UCLA), for proposing the relationship between the effective radiative aperture and optimal cell size in the antenna arrays, Prof. L. Kempel, Michigan State University, East Lansing, for the insightful discussion of the effect of the cell size on the frequency response, and Prof. A. Mortazawi, The University of Michigan at Ann Arbor, for providing the hard horns for the measurement setup.

REFERENCES

[1] B. A. Munk, *Frequency Selective Surfaces*. New York: Wiley, 2000.
[2] T. K. Wu, *Frequency Selective Surfaces and Grid Arrays*. New York: Wiley, 1995.
[3] A. Abbaspour-Tamijani, B. Schoenlinner, K. Sarabandi, and G. M. Rebeiz, "A new class of bandpass frequency selective structures," in *IEEE AP-S Int. Symp. Dig.*, Columbus, OH, June 2003, pp. 817–820.
[4] S. C. Ortiz, J. Hubert, L. Mirth, E. Schlecht, and A. Mortazawi, "A high-power Ka-band quasi-optical amplifier array," *IEEE Trans. Microwave Theory Tech.*, vol. 50, pp. 487–497, Feb. 2002.
[5] E. Fotheringham, S. Romisch, P. C. Smith, D. Popovic, and Z. Popovic, "A lens antenna array with adaptive optical processing," *IEEE Trans. Antennas Propagat.*, vol. 50, pp. 607–617, May 2002.
[6] C. J. Larson, "Modified center layer metallic bipolar radome design," Electro Science Lab., Ohio State Univ., Columbus, OH, Tech. Rep. ASAL-TR-78-28, 1978.
[7] R. Pous and D. M. Pozar, "A frequency-selective surface using aperture couples microstrip patches," *IEEE Trans. Antennas Propagat.*, vol. 39, pp. 1763–1769, Dec. 1991.
[8] G. L. Matthaei, L. Young, and E. M. T. Jones, *Microwave Filters: Impedance-Matching Networks, and Coupling Structures*. New York: McGraw-Hill, 1964.
[9] R. S. Elliott, *Antenna Theory and Design*, revised ed. New York: Wiley, 2003.
[10] J. K. A. Everard and K. K. M. Cheng, "High performance direct coupled bandpass filters on coplanar waveguide," *IEEE Trans. Microwave Theory Tech.*, vol. 41, pp. 1568–1573, Sept. 1993.
[11] A. Abbaspour-Tamijani, L. Dussopt, and G. M. Rebeiz, "Miniature and tunable filters using MEMS capacitors," *IEEE Trans. Microwave Theory Tech.*, vol. 51, pp. 1878–1885, July 2003.
[12] A. D. Margomenos, "Three dimensional integration and packaging using silicon micomachining," Ph.D. dissertation, Dept. Elect. Eng. Comput. Sci., Univ. Michigan at Ann Arbor, Ann Arbor, MI, 2003.
[13] B. C. Deckman, "Active quasi-optics and measurements," Ph.D. dissertation, Dept. Elect. Eng., California Inst. Technol., Pasadena, CA, 2000.
[14] N. Gagnon, J. Shaker, P. Berini, L. Roy, and A. Petosa, "Material characterization using a quasi-optical measurement system," *IEEE Trans. Instrum. Meas.*, vol. 52, pp. 333–336, Apr. 2003.
[15] M. A. Ali, S. C. Ortiz, T. Ivanov, and A. Mortazawi, "Analysis and measurement of hard-horn feeds for the excitation of quasi-optical amplifiers," *IEEE Trans. Microwave Theory Tech.*, vol. 47, pp. 479–487, Apr. 1999.
[16] G. F. Engen and C. A. Hoer, "Thru-reflect-line: An improved technique for calibrating the dual six-port automatic network analyzer," *IEEE Trans. Microwave Theory Tech.*, vol. MTT-27, pp. 987–993, Dec. 1979.

Abbas Abbaspour-Tamijani (S'00–M'04) received the B.S. and M.S. degrees from the University of Tehran, Tehran, Iran, in 1994 and 1997, respectively, and the Ph.D. degree from The University of Michigan at Ann Arbor, in 2003, all in electrical engineering.

From 1997 to 1999, he was an RF and Antenna Engineer in the telecommunication industry, during which time he was involved in the design of antennas and RF circuits and subsystems. From 1999 to 2000, he was with the Antenna Laboratory, University of California at Los Angeles (UCLA), where he was involved with the design of slot arrays and feed systems for space-borne reflector antennas. In Fall 2000, he joined The Radiation Laboratory, The University of Michigan at Ann Arbor. He is currently a Senior RF Engineer with Motia Inc., Pasadena, CA. In Fall 2004, he will join Arizona State University, Tempe, as an Assistant Professor of electrical engineering. His research area includes RF microelectromechanical systems (MEMS), phased arrays, focal plane scanning systems, passive and active quasi-optics, and multifunctional integrated devices for RF front-ends.

Kamal Sarabandi (S'87–M'90–SM'92–F'00) received the B.S. degree in electrical engineering from the Sharif University of Technology, Tehran, Iran, in 1980, and the M.S.E. and Ph.D. degrees from The University of Michigan at Ann Arbor, in 1986 and 1989, respectively, both in electrical engineering.

He is currently the Director of The Radiation Laboratory and a Professor with the Department of Electrical Engineering and Computer Science, The University of Michigan at Ann Arbor. His research areas of interests include microwave and millimeter-wave radar remote sensing, electromagnetic-wave propagation, and antenna miniaturization. He possesses 20 years of experience with wave propagation in random media, communication channel modeling, microwave sensors, and radar systems and is leading a large research group including four research scientists and 12 Ph.D. and two M.S. students. Over the past ten years, he has generated 20 Ph.D. students. He was the Principal Investigator of numerous projects sponsored by the National Aeronautics and Space Administration (NASA), Jet Propulsion Laboratory (JPL), Army Research Office (ARO), Office of Naval Research (ONR), Army Research Laboratory (ARL), National Science Foundation (NSF), Defense Advanced Research Projects Agency (DARPA), and numerous industries. He has authored numerous book chapters and over 115 papers appearing in refereed journals on electromagnetic scattering, random media modeling, wave propagation, antennas, microwave-measurement techniques, radar calibration, inverse-scattering problems, and microwave sensors. He has also authored or coauthored over 230 papers and invited presentations in many national and international conferences and symposia on similar subjects. He is listed in *Who's Who in American Men and Women of Science*, *Who's Who in America*, and *Who's Who in Electromagnetics*.

Dr. Sarabandi is a vice president of the IEEE Geoscience and Remote Sensing Society (GRSS), chairman of the Awards Committee of the IEEE GRSS, and a member of the IEEE Technical Activities Board Awards Committee. He is the associate editor of the IEEE TRANSACTIONS ON ANTENNAS AND PROPAGATION and the IEEE SENSORS JOURNAL. He is also a member of Commission F of URSI and The Electromagnetic Academy. He was the recipient of the Henry Russel Award from the Regent of The University of Michigan (the highest honor the University of Michigan bestows on a faculty member at the assistant or associate level), the 1999 GAAC Distinguished Lecturer Award presented by the German Federal Ministry for Education, Science, and Technology, which is given to approximately ten individuals worldwide in all areas of engineering, science, medicine, and law, and a 1996 Teaching Excellence Award presented by the Electrical Engineering and Computer Science Department, The University of Michigan at Ann Arbor. Over the past several years, joint papers presented by his students at a number of symposia [IEEE Antennas and Propagation Society (IEEE AP-S) Symposia (1995, 1997, 2000, and 2001); the IEEE International Geoscience and Remote Sensing Symposium (1999); and the IEEE Microwave Theory and Techniques Society (IEEE MTT–S) International Microwave Symposium (IMS) (2001)] have been the recipients of Student Prize Paper Awards.

Gabriel M. Rebeiz (S'86–M'88–SM'93–F'97) received the Ph.D. degree in electrical engineering from the California Institute of Technology, Pasadena.

He is a Full Professor of electrical engineering and computer science (EECS) at The University of Michigan at Ann Arbor. His research interests include applying MEMS for the development of novel RF and microwave components and sub-systems. He is also interested in SiGe RF integrated-circuit (RFIC) design, and in the development of planar antennas and millimeter-wave front-end electronics for communication systems, automotive collision-avoidance sensors, and phased arrays.

Prof. Rebeiz was the recipient of the 1991 National Science Foundation Presidential Young Investigator Award and the 1993 URSI International Isaac Koga Gold Medal Award. He was selected by his students as the 1997–1998 Eta Kappa Nu EECS Professor of the Year. In October 1998, he was the recipient of the Amoco Foundation Teaching Award, given annually to one faculty member of The University of Michigan at Ann Arbor for excellence in undergraduate teaching. He was the corecipient of the IEEE 2000 Microwave Prize. In 2003, he was the recipient of the Outstanding Young Engineer Award of the IEEE Microwave Theory and Techniques Society (IEEE MTT-S) and a Distinguished Lecturer for the IEEE MTT-S.